TAO, Supplementary Issue, 63-84, March 1999

Sensor Calibration of the Ocean Color Imager

Wei-Song Lin[1], Jenn-Yii Wu[1], Heng-Je Chiu[1],
Chun-Sheng Chen[1] and Yu-Jen Chang[1]

(Manuscript received 4 November 1998, in final form 18 January 1999)

ABSTRACT

Ocean Color Imager (OCI) aboard the ROCSAT-1 satellite is a multi-spectral imaging spectrometer for observing pigment distribution in low-latitude oceans. Sensor calibration contributes to characterization of its radiometric response and to the development of a processing segment for recovering the at-sensor radiance data. The major characteristics of OCI are presented. A mathematical model is developed to approximate the radiometric response of OCI and the corresponding parameters are initially identified by pre-flight calibration and adapted in-flight by a method of cross-platform calibration. The procedure of the pre-flight calibration is described and the results are shown. The cross-platform in-flight calibration compares the radiance data with those measured by the vicarious orbital sensor over the cross points so that performance degradation or parameter change in OCI will not bias the sensor calibration. The difficulties in spectral matching, spatial resolution, sun-sensor geometry, radiometric compatibility, and data set registration have been considered. An algorithm of the parameter adaptation and data conversion has been developed and implemented.

(Keywords: Ocean color, Remote sensing, Radiometric calibration, Satellite)

1. INTRODUCTION

Ocean Color Imager (OCI) aboard the ROCSAT-1 satellite is a product of the National Space Program Office (NSPO) of the National Science Council (NSC) and has been built by the NEC Corporation. Technically OCI is an all-refractive, pushbroom and nadir-viewing imaging spectrometer designed to investigate ocean surface pigment distribution in low-latitude oceans ($\pm 35°$) by measuring six spectral bands in the visible and near-infrared spectrum. Pigment distribution data on a large scale is expected to contribute an understanding of ocean dynamics, chlorophyll variation, and oceanic primary production. The information containing radiance backscattered out of the water and transmitted to the top of the atmosphere is only a

[1]Institute of Electrical Engineering, National Taiwan University, Taiwan, ROC

small portion of the radiance measured by a space-borne ocean color sensor (Gordon, 1998). To achieve the water-leaving radiance, the OCI data requires several levels of radiometric calibration. The sensor calibration converts the measured digital counts to the at-sensor radiance data (Schowengerdt, 1997), the atmospheric correction transforms the at-sensor radiance data to the radiance at the ocean's surface, and the surface correction removes the radiance reflected directly from the ocean's surface to leave the water-leaving radiance. For sensor calibration one needs to have a radiometric model and to identify the corresponding parameters both in pre- and in-flight stages (Rao and Chen, 1994). The pre-flight calibration and validation activities for the OCI were executed at the NEC Corporation in Yokohama, Japan for sensor levels and at the NSPO in Taiwan for integrating into the ROCSAT-1 satellite. Using the design and testing results, the authors have elaborated the radiometric model and pre-flight parameters, a method of cross-platform in-flight parameter adaptation, and an algorithm and computer software to convert the OCI output into the at-sensor radiance data. Variations in the offset and degradation in the performance of the optics with time in orbit have been considered. This article is dedicated to describing the proposed method of sensor calibration and to summarizing the major parameters and characteristics of OCI for the follow-up applications.

In the second section, the characteristics of the OCI flight model are summarized with detailed values. The third section develops an approximate radiometric model of OCI. The fourth section describes the procedure for the pre-flight calibration and identifies the model parameters. In the fifth section, a cross-platform and a cross-band in-flight calibration for OCI are proposed. The sixth section describes the implemented algorithm of the sensor calibration. The last section is the conclusion.

2. CHARACTERISTICS OF OCI

OCI is basically an electro-optical assembly with four independent telecentric dioptric systems to accommodate seven spectral bands as shown in Figure 1 (a) and (b), respectively as the schematic view and optics (Narimatsu et al., 1997a). The seven bands are actually six plus a redundant one. The band selections considered the spectral characteristics of in-water optical constituents, spectral transmittance of the atmospheric constituents and data fusion with other space-borne ocean color sensors. As shown in Table 1, the six bands are specified to center at

Table 1. Bands of OCI.

Band	$\overline{\lambda}$ (nm)	$\Delta\lambda$ (nm)	Phenomenon
1	443	20	Chlorophyll Absorption (blue)
2	490	20	Pigment
3	510	20	Chlorophyll Absorption (green)
4/7	555	20	Hinge point, Sediments (yellow)
5	670	20	Aerosol Correction (red)
6	865	40	Aerosol Correction (NIR)

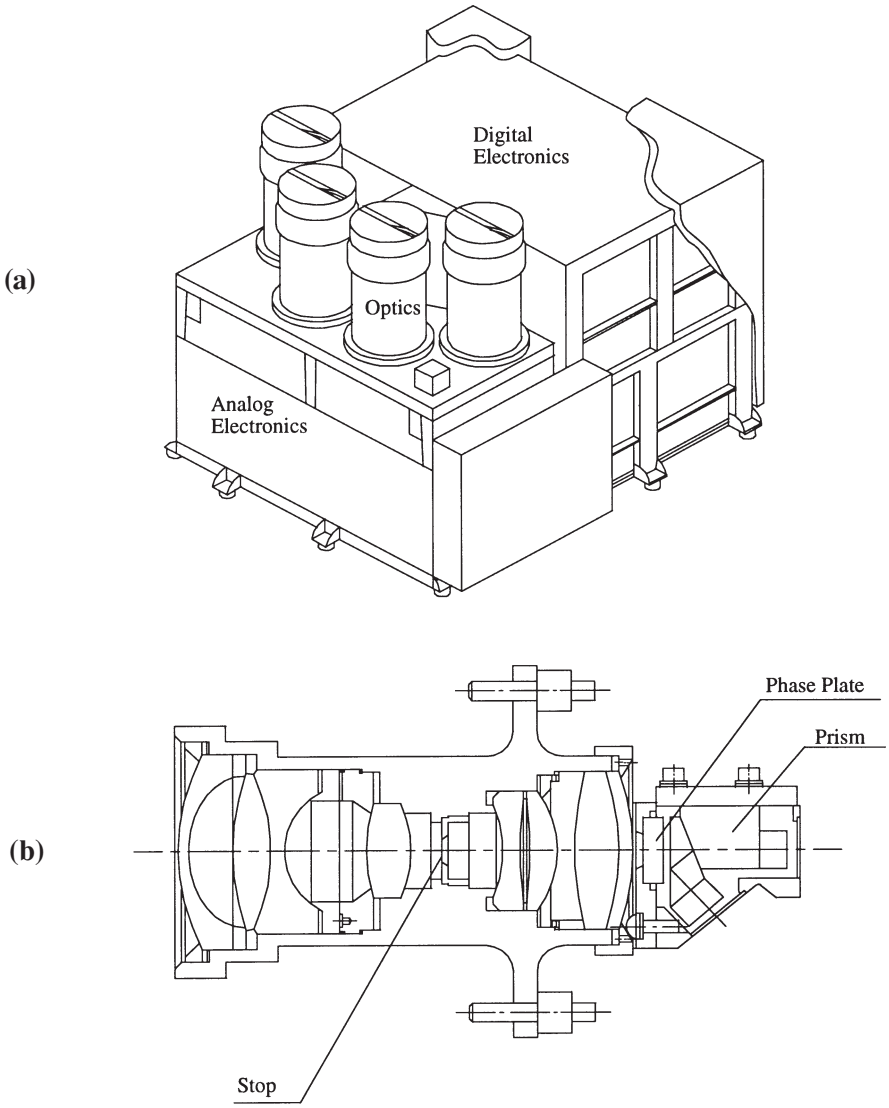

Fig. 1. (a) A schematic view of the OCI, (b) the telecentric dioptric optics.

443, 490, 510, 555, 670, and 865 nm, respectively. The redundant band is centered at 555 nm and denoted as Band 7. The desired bandwidth for Bands 1~5 and 7 is 20 nm, and Band 6 is 40 nm.

Physical implementation of the OCI is subject to the deployment of total mass, envelope and other resources on the ROCSAT-1 satellite. To meet the specifications without violating the deployment, Bands 1 and 3, as shown in Figure 1(b), were implemented to draw radiance from one single telescope. A lens system and a phase plate focus and depolarize the light

beam, respectively, and a prism beam splitter distributes the incoming radiance to the two linear charge-coupled device (CCD) arrays assembled on each of the two focal planes. The interference filter in front of each CCD array determines the center wavelength and bandwidth of the corresponding band. Bands 2 and 4, and Bands 5 and 6 form another two pairs and are built in the same way. Band 7, which is a backup of Band 4, has a stand-alone telescope with the same structure. The four sets of optics and seven detector assemblies were manufactured and aligned accurately to give spectral registration errors no larger than 0.65 IFOV (instantaneous field-of-view) along track and 0.97 IFOV cross track. The construction and testing of the OCI flight model has been completed and Table 2 summarizes its major parameters and characteristics (Narimatsu et al., 1997b).

The TH7811 (Thomson-CSF) CCD array has been chosen as the detector for each band. This component has 1728 cells arranged as a linear array and has the particular function of anti-blooming control. The photosensitive area of each cell is approximately $13 \times 13 \mu m^2$. In the OCI pushbroom scanning, the cells of each band are organized as shown in Figure 2 to give a total of 896 pixels with 832 double-cell pixels (dp) separated equally on both sides and 64 single-cell pixels (sp) located at the center part. A double-cell pixel with 115.8msec integration time interval is specified to give an approximately $800 \times 800 m^2$ footprint at nadir in a 600km orbit. In the same situation, a single-cell pixel will have only $400 \times 800 m^2$ footprint. All 896 pixels combined with the wide field-of-view optics and the motion of the satellite are expected to scan with a swath width of no less than 690km in a 600km orbit. Table 2 presents the detailed swath values obtained by physical implementation. The OCI achieves high performance in the across track modulation transfer function (MTF), but the across track MTF in Band 6 is exceptionally low due to its larger bandwidth. The high signal to noise ratio (SNR), which is obtained mainly by a very low noise electronic implementation, combined with the 12-bit digitization, ensures the accuracy of the OCI data.

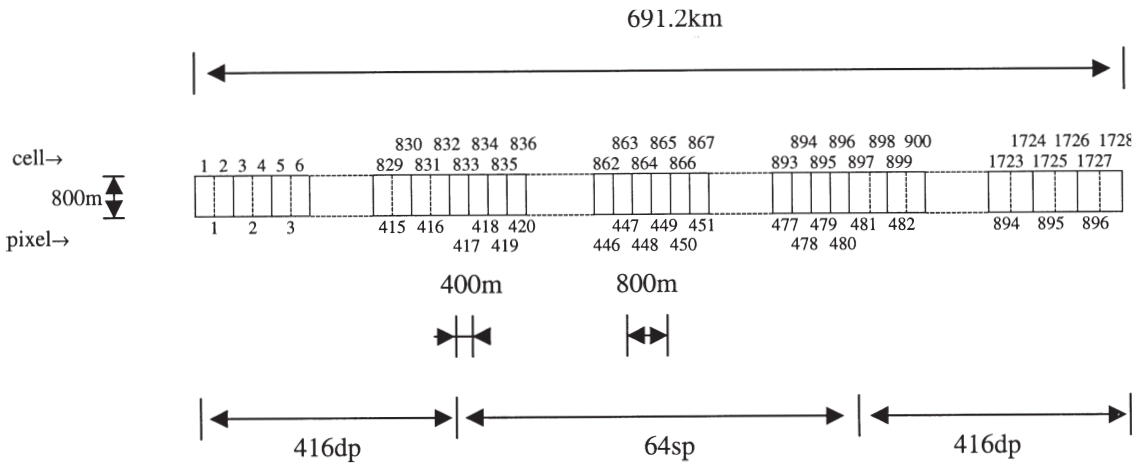

Fig. 2. Organization of CCD cells.

Table 2. Major parameters and characteristics of OCI.

Instrument characteristics	
Imaging method	pushbroom scanning
Optics	four-telecentric dioptric systems (lens system)
Dimension	378.8(X)+348.6(Y)+342.0(Z) mm
Weight	15.2 kg
Power consumption	peak: 33W, standby: 17.4 W
Design life	2 years in orbit
Reliability	0.991 7 bands operating at the end of 2 years in orbit (3% duty cycle)
Orbit	incline 35^0, altitude 600km period 96.7 min., speed 7.56 km/sec
Operating modes	FB(1~7), NI-A(1~6), NI-B(1~3, 5~7), RGB(1,3,5), CA(4,7)
Gain selection	normal=1.0, low=0.5, high=2.0 (6.0 for Band 7)
Image data rate (limit)	<654.8 kbps (655.5kbps)
Detectors	linear CCD arrays, 1728 cells, $13\mu m \times 13\mu m$
Pixels per band	896 pixels (832 double +64 single cells)
Integration time interval	115.8 msec
Signal digitization	12 bits / pixel
Absolute radiance accuracy	5% or better at BOL
Spectral co-registration error	along track: ≤ 0.65 IFOV
(with respect to Band 4)	cross track: ≤ 0.97 IFOV
Polarization sensitivity	≤ 2%
Anti-blooming	≤ 10% of V_{sat} at the 10^{th} pixel ($E=6xE_{sat}$)

Band characteristics							
Band	B1	B2	B3	B4	B5	B6	B7
Swath width (km) (h=600 km)	701.6	702.2	702.2	702.4	702.0	702.3	702.1
FOV	$60^0$37' 42.3"	$60^0$40' 11.1"	$60^0$40' 5.3"	$60^0$40' 57.0"	$60^0$39' 26.4"	$60^0$40' 36.6"	$60^0$39' 57.0"
GIFOV (m) (h=600km at nadir)	807.5	808.4	806.3	807.5	808.1	806.6	806.9
IFOV (at nadir)	4'37.6"	4'37.9"	4'37.2"	4'37.6"	4'37.8"	4'37.3"	4'37.4"
Center wavelength (nm) (specification)	444.0 (443)	491.6 (490)	511.9 (510)	554.6 (555)	670.0 (670)	868.9 (865)	554.7 (555)
Bandwidth (nm) (specification)	20.0 (20.0)	20.1 (20.0)	19.6 (20.0)	18.5 (20.0)	18.5 (20.0)	40.3 (40.0)	18.5 (20.0)
MTF (across track) (pixel no. 416)	0.77	0.78	0.78	0.76	0.66	0.53	0.79
MTF (along tack) (pixel no. 416)	0.56	0.60	0.56	0.57	0.58	0.55	0.58
SNR (pixel no. 416)	899.9	934.4	914.9	790.4	891.1	799.3	845.1
Mean radiance	84.1	65.6	56.4	45.7	24.6	10.9	45.7
Saturation radiance	132.5	105.0	90.8	74.4	42.0	21.3	74.4
Out of band spectral rejection (%)	0.10	0.22	0.09	0.11	0.19	0.07	0.09

3. APPROXIMATE RADIOMETRIC MODEL OF OCI

OCI is an electro-optical sensor that converts the at-sensor radiance into appropriate digital counts. According to the design and physical implementation, its signal flow can be represented as shown in Figure 3. The at-sensor radiance is transformed sequentially by the telescope, detector, analog electronics, multiplexer, gain selector, and analog to digital converter to obtain the digital counts. Telescope A provides the radiance for Bands 1 and 3 that have stand-alone detectors and analog electronic circuits. The same situations occur in Telescope B for Bands 2 and 4, and Telescope C for Bands 5 and 6. The signals picked up by the detectors of the seven bands are sequentially multiplexed to a gain selector and an analog to digital converter. The gain selector provides normal (1.0), low (0.5), and high (2.0 for Bands 1~6, 6.0 for Band 7) gains in compliance with the signal level. To investigate the radiometric response of a single spectral band, the key components affecting the performance are identified and shown in Figure 4 with the major factors being indicated. The blocks in heavy line represent the common units of the seven bands. The major factors that affect the radiometric or instrument response of OCI exist mainly in components such as the optics, the detector, and the electronics. In the optics, these factors are characterized by the transmission of the lens, MTF, field-of-view (FOV), straylight of the optical assembly, depolarization of the phase plate, and center wavelength ($\bar{\lambda}$) and bandwidth ($\Delta\lambda$) of the interference filters. The responsivity and dark signal of the CCD are the most important factors to be considered in the optical to electrical conversion. The analog and digital electronics transform the electric signal into appropriate digital counts with response function characterized by the amplifier or buffer gain and bias,

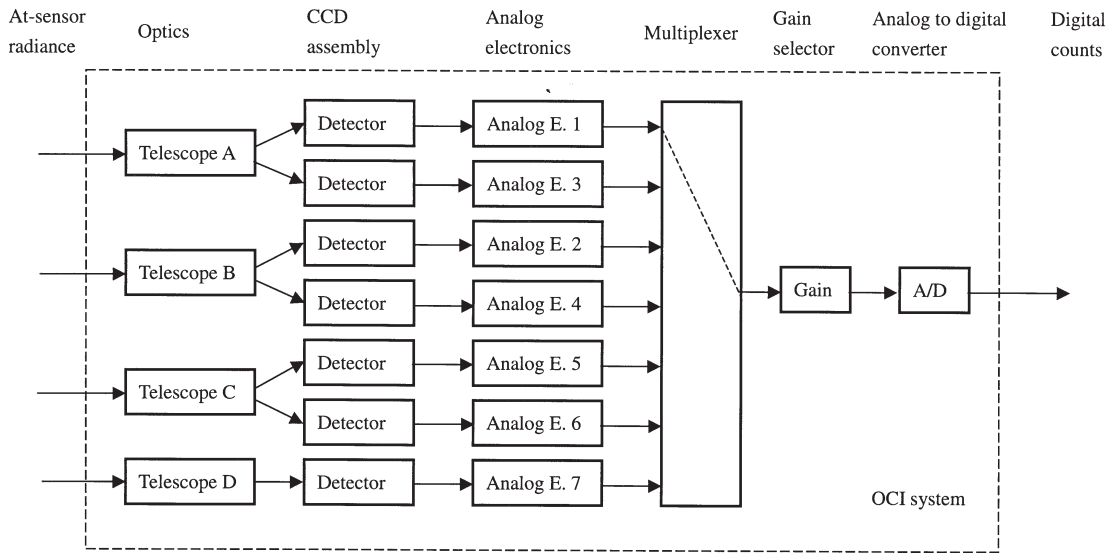

Fig. 3. Signal flow and main components of the OCI, where each numeral denotes the corresponding band.

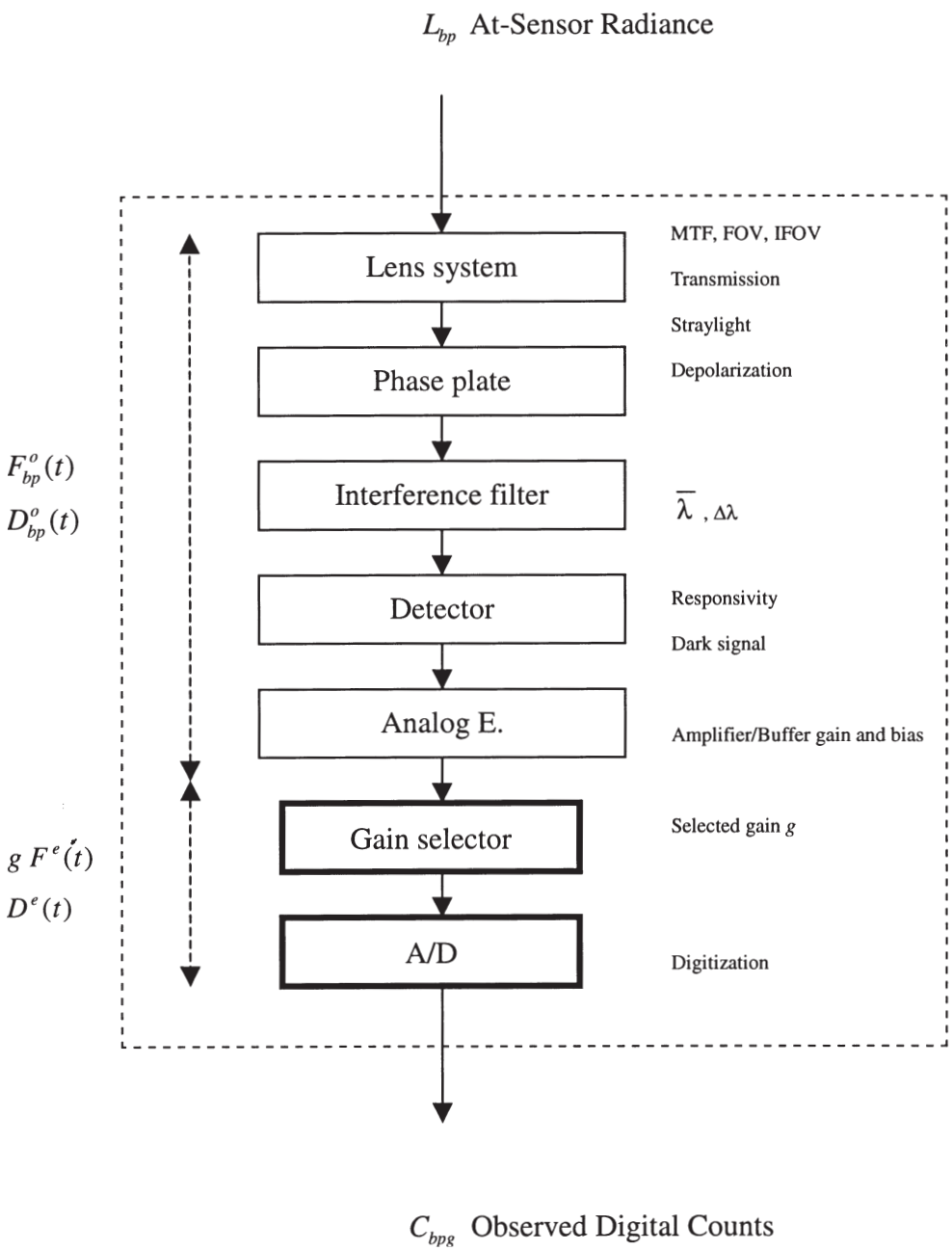

Fig. 4. Major factors affecting the performance of a single band.

digitization, and noise. Since these factors characterize the response functions of the optics, the detector, the electronics as well as the whole OCI instrument, they were specified in the requirements of the OCI in detail. The manufacturer built the OCI with appropriate material,

components, construction and testing procedure to achieve the desired result (NSPO, 1993). Therefore the engineering phase for building OCI was complicated and difficult, but fortunately the construction and testing have been successfully completed and all the design data, as well as the testing data, are available.

The overall instrument response function of OCI is theoretically the convolution of the component response functions (Schowengerdt, 1997). However to simplify the data conversion and parameter calibration, it is assumed that, for an integration time interval, the spectral response of OCI is an average constant over an effective spectral band, and that the spatial response is an average constant over the effective area of a detector element. Thus the band-, space- and time-integrated at-sensor radiance measured by OCI can be represented by the following equation:

$$L_{bp}(t) = \iiint_{\Delta\tau\Delta A\Delta\lambda} L(\lambda, A, \tau)\, d\lambda\, dA\, d\tau \tag{1}$$

where L_{bp} denotes the measured radiance at a particular CCD pixel p in band b, the (t) is used to stamp the time of measurement, $\Delta\lambda$ is the effective spectral band, ΔA is the effective area of an CCD pixel, and $\Delta\tau$ is the integration time interval. By referring to Figure 4, the radiometric response of the OCI can be approximated mathematically by a linear, slow time-varying system as follows:

$$C_{bpg}(t) = gF^e(t)[F^o_{bp}(t)L_{bp}(t) + D^o_{bp}(t)] + D^e(t) \tag{2}$$

where C, F, and D denote, respectively, the digital counts, sensor gain and offset, and where g is the selected gain. The subscripts denote a particular band b, pixel p, and selected gain g, respectively, and the superscripts o and e represents roughly the optical-related and common electronic portions of OCI. The terms on the right hand side of (2) can be rearranged as follows:

$$C_{bpg}(t) = gF_{bp}(t)L_{bp}(t) + D_{bpg}(t) \tag{3}$$

where

$$F_{bp}(t) = F^e(t)F^o_{bp}(t) \tag{4}$$

and

$$D_{bpg}(t) = gF^e(t)D^o_{bp}(t) + D^e(t) \tag{5}$$

(3) can be rewritten by referring to the pre-flight sensor gain as follows:

$$C_{bpg}(t) = \alpha_{bp}(t)gF_{bp}(t_0)L_{bp}(t) + D_{bpg}(t) \tag{6}$$

where t_0 denotes the time of pre-flight calibration, and

$$\alpha_{bp}(t) = \frac{F_{bp}(t)}{F_{bp}(t_0)} \tag{7}$$

is designated as the relative sensor gain. Equations (6) and (7) form an approximate radiometric model for the calibration and parameter adaptation of OCI. Using this model, the pre-flight calibration needs to identify $F_{bp}(t_0)$ and $D_{bpg}(t_0)$, and the in-flight calibration is requested to estimate $\alpha_{bp}(t)$ and $D_{bpg}(t)$ periodically or frequently during OCI's lifetime.

4. PRE-FLIGHT PARAMETERS OF OCI

With the model described by (6) and (7), and assuming the OCI parameters to vary very slowly with time, then in the pre-flight calibration we have

$$\alpha_{bp}(t_0) = 1.0 \tag{8}$$

and the approximate radiometric model becomes

$$C_{bpg}(t) = gF_{bp}(t_0)L_{bp}(t) + D_{bpg}(t_0) \tag{9}$$

where g=1.0 is a convenient choice. Pre-flight parameters of OCI at room temperature were obtained in Oct. 1997. The primary standard of radiance was a copper point blackbody source at 1084.62^{0}C. The secondary standard of radiance was a variable-temperature transfer blackbody operated at between 800^{0}C ~1500^{0}C. The OCI integrating sphere has specifications as shown in Table 3. The sphere was calibrated in Nov. 1996 relative to the primary standard using the variable-temperature transfer blackbody and a double grating monochromator. The procedure is described in (Narimatsu et al., 1997c) and briefly is as follows. The radiance of the primary standard was calculated by using Planck's law. A monochromator was used to compare the spectral radiance of the variable-temperature transfer blackbody with the primary standard. Then the variable-temperature transfer blackbody was transported to the working place and applied to validate the radiance of the sphere. For Bands 1~4, and Band 7, the variable-temperature transfer blackbody was set to 1372^{0}C, but for Bands 5 and 6 the temperature was at 957^{0}C.

In the calibration, OCI was kept at room temperature and set to normal gain and calibrated by observing a variety of output radiance of the sphere. The output radiance of the sphere

Table 3. Specifications of the OCI integrating sphere source.

Inner diameter	2 m						
Aperture diameter	500 mm						
Coating on inner wall	Barium sulfate						
Lamp configuration	26 lamps, 0~100V dc ± 0.01%						
Monitor detector	Silicon photodiode with infrared blocking filter						
Cooling	Air circulation with fans						
Band	1	2	3	4	5	6	7
No. of lamps turned on	26	26	26	26	13	13	26
Lamp voltage [V]	90.0	77.0	70.0	58.0	46.0	25.8	58.0
Temp. of cal. blackbody [^{0}C]	1372	1372	1372	1372	957	957	1372

Table 4. Output radiance of the integrating sphere for the OCI calibration.

Point	Band 1	Band 2	Band 3	Band 4, 7	Band 5	Band 6
1	93.90	99.51	87.86	69.75	39.34	21.49
2	86.77	91.92	81.11	64.35	36.47	19.94
3	72.26	76.56	67.55	53.53	30.58	16.71
4	57.88	61.28	54.12	42.87	24.15	13.21
5	43.27	45.78	40.39	31.97	18.30	9.97
6	28.98	30.73	27.12	21.48	11.92	6.51
7	14.15	14.98	13.20	10.43	6.04	3.30
8	0.00	0.00	0.00	0.00	0.00	0.00

Unit: $w/(m^2 \cdot Sr \cdot \mu m)$

applied to calibrate OCI is listed in Table 4. The radiance was selected to test eight points with magnitudes less than the saturation radiance of each band. Recording the digital counts obtained by OCI corresponding to the applied radiance and applying linear regression can approximate the parameters in (9). The whole set of the pre-flight sensor gains, $F_{bp}(t_0)$, is depicted by curves, as shown in Figure 5. The difference between single- and double-cell pixels results in the low sensor gains in the center portions of the curves. The gain values for each

Table 5. Pre-flight model parameters corresponding to pixel numbers 1, 416 and 896 (t_0=1997.10, g=1.0).

Band	CCD	Pixel no. 1		Pixel no. 416		Pixel no. 896	
	^{0}C	*F*	*D*	*F*	*D*	*F*	*D*
1	30.7	21.27	85.22	25.50	87.63	20.45	84.85
	10.1		48.10		47.98		47.98
2	31.3	27.28	94.70	33.35	103.28	27.03	93.30
	9.9		47.63		47.65		47.43
3	28.4	31.84	91.80	38.54	98.25	31.24	88.20
	10.5		48.48		48.03		47.83
4	31.4	28.72	94.09	35.89	95.78	28.14	92.59
	10.0		47.73		47.48		47.48
5	28.8	69.07	90.99	85.86	90.67	70.65	85.27
	10.0		46.95		44.60		46.40
6	28.8	126.05	83.10	155.28	87.21	122.69	75.78
	9.7		46.70		46.48		45.98
7	29.6	32.91	84.89	40.40	87.99	30.64	81.79
	10.0		44.10		43.85		43.73

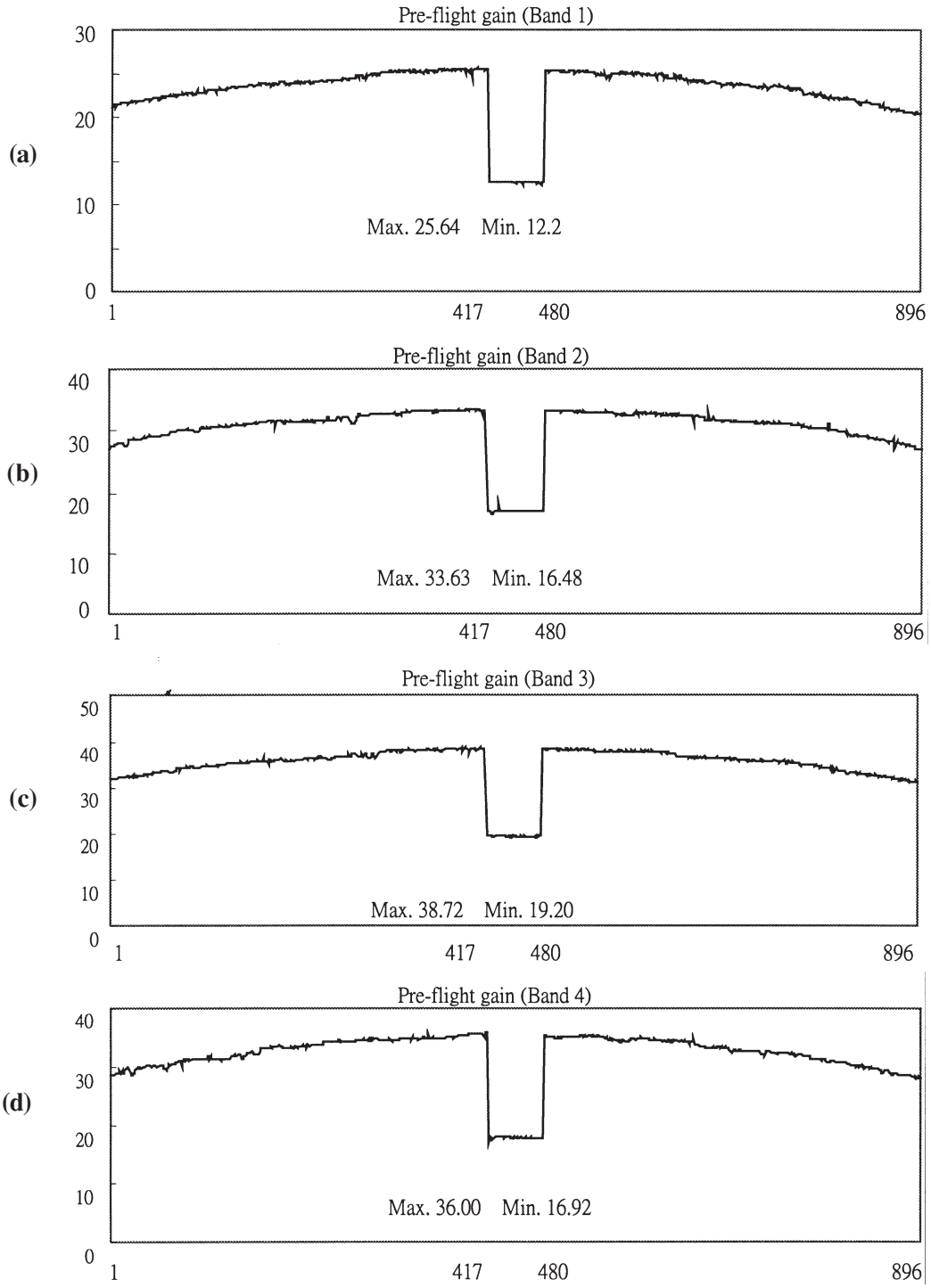

Fig. 5. Plots of pre-flight sensor gains against pixel numbers, (a) Band 1, (b) Band 2, (c) Band 3, (d) Band 4, (e) Band 5, (f) Band 6, and (g) Band 7.

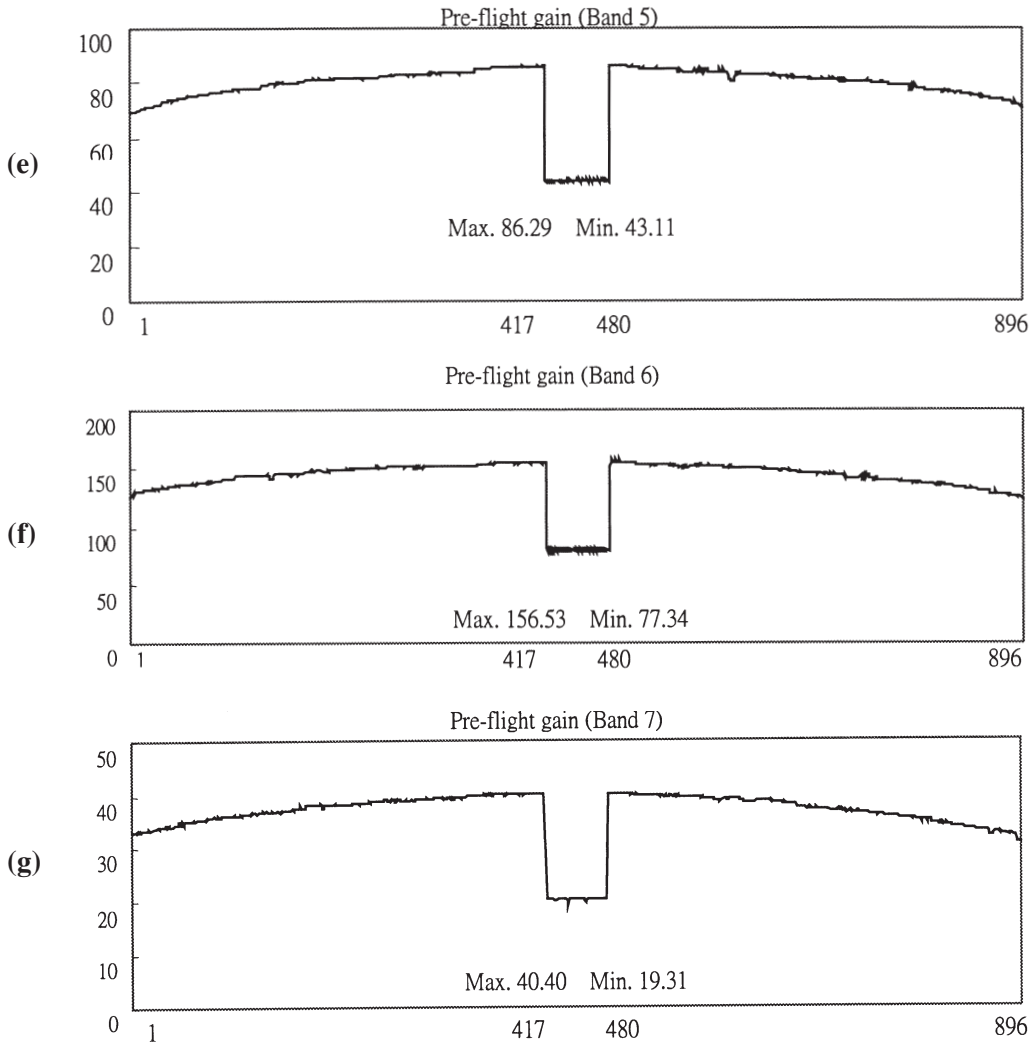

(Fig. 5. continued)

band at pixels 1, 416 and 896 are listed in Table 5 and labeled *F* (Narimatsu et al., 1997c). Since CCD is temperature sensitive, when OCI is in normal observation, the temperature of each CCD array will be controlled to within 10 ± 3^0C. Therefore, in spite of the pre-flight sensor gains being measured only at room temperature, the offset has been further measured for the CCD arrays being controlled at around 10^0C. The complete set of pre-flight offsets was measured for each band, pixel, and selected gain by the NSPO in July 1998 after OCI was integrated into the ROCSAT-1 satellite. Table 6 lists the mean values and standard deviations of the pre-flight offsets. Table 5 compares the offsets, labeled *D*, with the CCD arrays being operated at room and controlled temperatures, respectively.

Table 6. Mean and standard deviation of the offsets.

Band	Gain selection	CCD ^{0}C	Double-cell pixels		Single-cell pixels	
			Mean offset	Standard deviation	Mean offset	Standard deviation
1	1.0	10.0	47.981	0.291	42.198	0.332
2	1.0	10.3	47.981	0.291	42.198	0.332
3	1.0	10.3	47.528	0.347	42.128	0.246
4	1.0	10.3	48.190	0.324	42.316	0.224
5	1.0	10.1	47.010	0.216	39.656	0.298
6	1.0	9.7	46.804	0.181	41.488	0.223
7	1.0	10.8	45.298	0.248	39.308	0.271
1	2.0	9.7	98.422	0.417	85.446	0.650
2	2.0	8.3	97.183	0.439	85.818	0.282
3	2.0	10.2	99.693	0.553	87.136	0.458
4	2.0	8.4	97.510	0.385	86.206	0.431
5	2.0	9.6	98.107	0.471	84.918	0.443
6	2.0	9.3	98.330	0.404	86.846	0.375
7	6.0	8.7	282.520	1.248	249.93	1.566
1	0.5	9.6	25.858	0.096	23.158	0.145
2	0.5	8.2	22.868	0.103	21.399	0.216
3	0.5	10.1	22.423	0.203	20.813	0.187
4	0.5	8.3	21.493	0.144	19.978	0.134
5	0.5	9.5	21.451	0.173	17.883	0.155
6	0.5	9.2	21.411	0.147	19.206	0.119
7	0.5	8.6	19.947	0.063	17.682	0.180

5. IN-FLIGHT CROSS-CALIBRATION

Although OCI has been designed without any moving component to achieve reliability as high as 0.991 at the end of two years in orbit, one major cause of change in the radiometric response is the degradation of optical transmittance due to exposure to environmental radiation and contamination of the optics by outgassing. Another possibility is the mechanical shift of the optical assembly during launch. Therefore the continuity of the pre-flight calibration data with the in-flight data, and the long-term variations in the performance should be monitored. Using the radiometric model (6) and (7), if the at-sensor radiance data is available, the in-flight relative sensor gain can be assessed by

$$\alpha_{bp}(t) = \frac{\widehat{C}_{bpg}(t) - \widehat{D}_{bpg}(t)}{gF_{bp}(t_0)\widehat{L}^{v}_{bp}(t)} \tag{10}$$

where '^' denotes the measured value, $\hat{C}_{bpg}(t)$ is the digital counts obtained by OCI, $\hat{D}_{bpg}(t)$ is the measured offset, and $\hat{L}^{v}_{bp}(t)$ is the known at-sensor radiance data.

5.1 Cross-platform In-flight Calibration

Since the offset can be estimated by observing the night side of the earth, all that remains is to choose an appropriate way or multiple ways to provide the at-sensor radiance data. For this purpose, on-board calibration using a lamp light source, blackbody radiator, moonlight or diffused sunlight (Ono et al., 1996), and many vicarious and cross-calibration methods have been considered for orbital sensors (Che et al., 1991; Gordon, 1998; Slater et al., 1987). Among them, assessing the at-sensor radiance by vicarious measurements of the reflectance or radiance of some target site has been used with great success. Here, since several ocean color sensors are expected to operate simultaneously within OCI's mission time (Hooker et al., 1992; Salomonson et al., 1989), apart from using reflectance-based or airborne sensor measurement, another important approach is to calibrate the OCI with respect to the calibrated radiance data measured near in time by these orbital sensors. The difficulties resulting from differences in spectral matching, ground spatial resolution, and sun-sensor geometry (Che et al., 1991), and problems in radiometric compatibility and data set registration are investigated as follows:

a. Spectral matching

Table 7 shows the matching and partially overlapping spectral bands of several ocean

Table 7. Spectral matching among OCI, SeaWiFS, MODIS, OCTS and CZCS. Overlapping bands are listed in the same rows. The thick line blocks in a row indicate the matching bands. MODIS has 36 bands, but only ocean color bands are presented here. The unit of wavelength is in nm except where denoted.

OCI	OCTS	SeaWiFS	MODIS	CZCS
	402 - 422	402 - 422	407.5 – 422.5	
433 - 453	433 - 453	433 - 453	438 - 448	433 - 453
480 - 500	480 - 500	480 - 500	485 - 495	
500 - 520	510 - 530	500 - 520		510 - 530
			526 - 536	
545 - 565	555 - 575	545 - 565	550 - 560	540 - 560
660 - 680	655 - 675	660 - 680	662 - 672	660 - 680
			676 - 686	
				700 - 800
	745 - 785	745 - 785	745 - 755	
845 - 885	845 - 885	845 - 885	857.5 – 872.5	
	3.55 - 3.88 μm			
	8.25 - 8.8 μm			
	10.3 - 11.4 μm			
	11.4 - 12.5 μm			10.5 - 12.5 μm

color sensors by their specifications. The Ocean Color and Temperature Scanner (OCTS) on the ADEOS satellite is a product of the National Space Development Agency (NASDA) of Japan. It was launched in 1996, but failed to operate in orbit after February 1997. The Sea-viewing Wide Field-of-view Sensor (SeaWiFS) on the SeaStar satellite is a product of the National Aeronautics and Space Administration (NASA) Office of Space and Science Applications and Goddard Space Flight Center (GSFC) of the United States. SeaWiFS was successfully launched in 1997. The Moderate Resolution Imaging Spectroradiometer (MODIS) on the Earth Observing System's (EOS) AM-1 spacecraft being scheduled to be launched in 1998 is also a program of the NASA. The Coastal Zone Color Scanner (CZCS) on Nimbus-7 that is a pioneer of in-orbit ocean color sensing has ceased operating in 1986. As shown in Table 7, three of the OCTS bands match Bands 1, 2 and 6, and another three bands partially overlapping with Bands 3, 4 and 5 of the OCI. SeaWiFS has six bands nicely matching each OCI band. MODIS has five bands partially overlapping with 1, 2, 4, 5, and 6 of the OCI bands. CZCS has bands matching Bands 1, 4, and 5 the OCI. In spite of the partially overlapping bands, when taking the uncertainties in physical implementation into consideration, no bands can match each other perfectly. Table 2 shows the bandwidths of OCI implemented are slightly different from their specified values. So, selecting appropriate surface sites for cross-platform calibration should be considered to reduce the spectral mismatch uncertainties. However the nice matching of OCI with the SeaWiFS bands should release the selection of the surface sites to a maximum. In other words most of the open sea under the cross observations of OCI and SeaWiFS should meet the requirements. Homogeneous ground sites with uniform reflectance are another choice, except the saturation conditions of the detectors must be considered. For those with partially overlapping bands, such as MODIS, the selection of surface sites for the OCI cross-platform calibration is limited and spectral mismatch should be investigated carefully. Obviously SeaWiFS seems to be a good candidate for cross-platform in-flight calibration of OCI.

b. Ground spatial resolution

The resolutions at nadir are respectively $800 \times 800 m^2$ for a double-cell pixel of OCI, $1100 \times 1100 n^2$ for local area coverage (LAC) and $4500 \times 4500 m^2$ for global area coverage (GAC) of the SeaWiFS, and $1000 \times 1000 m^2$ for the ocean color bands of the MODIS. To account for the difference of ground spatial resolutions, multiple pixels of each instrument with the same ground coverage are compared for the cross-platform calibration. Assuming that $I^{OCI}J^{OCI}$ pixels (i.e. I pixels per line $\times$ J lines) at nadir of the OCI have the same ground coverage as I^vJ^v pixels of the cross-compared vicarious orbital sensor. For the OCI against the calibrated SeaWiFS LAC data, $I^{OCI}J^{OCI}=11\times11=121$ and $I^vJ^v=8\times8=64$ are appropriate choices. Similarly for the calibrated MODIS data $I^{OCI}J^{OCI}=5\times5=25$ and $I^vJ^v=4\times4=16$ are suitable values. Then the at-sensor radiance data corresponding to a double-cell OCI pixel can be assessed as an average of the vicarious measurements as follows:

$$\bar{L}^v_{bp}(t) = \frac{1}{I^{OCI}J^{OCI}} \sum_{j=1}^{J^v} \sum_{i=1}^{I^v} \hat{L}^v_{bp_{ij}}(t) \tag{11}$$

where '–' indicates averaging. Due to the atmosphere changes resulting from off-nadir observations of wide field-of-view instruments in different orbiting conditions like the OCI and SeaWiFS. Only the pixels at nadir obtained by measuring a homogeneous surface site with uniform reflectance can ensure the correctness of (11). Therefore pixel by pixel assessments of the at-sensor radiance data by this method is difficult. Considering decomposing the relative sensor gain as follows:

$$\alpha_{bp}(t) = \alpha_b(t)\alpha_p(t) \tag{12}$$

where $\alpha_b(t)$ and $\alpha_p(t)$ are termed respectively as band-common and pixel-dependent portions of the relative sensor gain. Precise assessments of the pixel-dependent portions for the OCI can only be done by pre-flight calibration. Vicarious calibration for this purpose based on surface measurements is difficult due to its pushbroom scanning with wild field-of-view. Fortunately except for changes in the responsivity of some CCD pixel and contamination of or damage at some optical component locally, the robust design of OCI should be able to ensure the pixel-dependent property to be kept steady, and for most of the cases

$$\alpha_p(t)=1.0 \tag{13}$$

is correct. Then the band-common portion can be estimated by using the following equations:

$$\alpha_b(t) = \frac{\bar{L}^{OCI}_{bp_{nadir}}(t)}{\bar{L}^{v}_{bp_{nadir}}(t)} \tag{14}$$

where

$$\bar{L}^{OCI}_{bp_{nadir}}(t) = \frac{1}{I^{OCI}J^{OCI}}\sum_{j=1}^{J^{OCI}}\sum_{i=1}^{I^{OCI}}[L^{OCI}_{bp_{ij}}(t)] \tag{15}$$

$$L^{OCI}_{bp_{ij}} = \frac{\hat{C}_{bp_{ij}g}(t) - \hat{D}_{bp_{ij}g}(t)}{gF_{bp_{ij}}(t_0)} \tag{16}$$

and p_{ij} for i=1,...,I^{OCI} and j=1,...,J^{OCI} represents the pixels at nadir. Referring to the architecture of OCI, the performance shift in the optics and electronic circuit units of a band will appear in the result of assessment by using (14).

c. Sun-sensor geometry

Sensors on different platforms will observe the target site under different illumination and viewing conditions that introduces atmospheric changes and surface bi-directional reflectance effects. The OCI orbit inclines 35^0 and has ground track crossing those with sun-synchronous orbits. To eliminate the effect of different sun-sensor geometry, an effective method is to do the cross-platform calibration by only comparing the data obtained near in time over the cross points.

d. Radiometric compatibility

The radiometric output of OCI, SeaWiFS, MODIS, and OCTS are calibrated in the laboratory using known sources of spectral radiance such as integrating spheres and blackbody

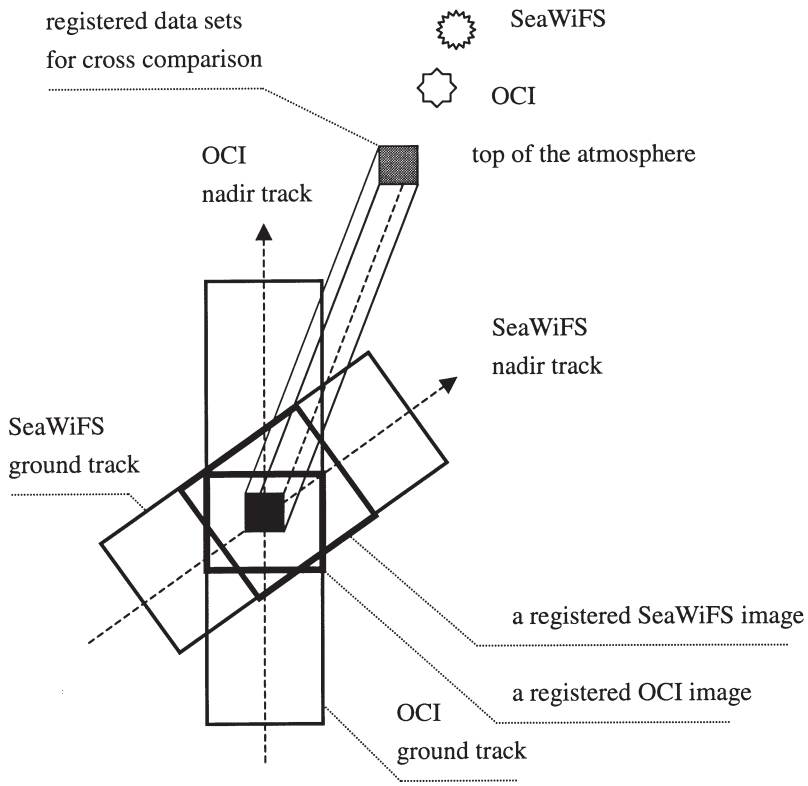

Fig. 6. A schematic representation of the image and data set registrations.

radiators. These sources refer to some primary standards maintained respectively by the United States and Japan. That means the same at-sensor radiance may result in unequal spectral data by each of the ocean color sensors. Therefore the compatibility of the output data of the cross-compared sensors has to be investigated before launch. On this purpose, a radiometric comparison was held in February 1995 to calibrate and validate the OCTS integrating sphere with respect to the SeaWiFS and MODIS measurements (Johnson et al., 1997). The OCTS integrating sphere measured by the NEC Corporation in Yokohama, Japan was reported between –2.7% and 3.9% (near zero by average) comparing with the measurements of spheres for calibrating the MODIS and SeaWiFS in the United States. Although OCTS has failed to operate since February 1997, the cross comparison remains to be an important reference to OCI. Because the same primary standard, integrating sphere and calibration method have been applied to calibrate the OCTS and OCI (Narimatsu et al., 1997c). This means the radiometric uncertainties of the OCTS with respect to the SeaWiFS and MODIS apply to OCI, and the compatibility of the spectral data among them are ensured.

e. Data set registration

According to the method of cross-platform calibration described in sub-section *b*, the

calibration requires data sets from around the cross point of the nadir tracks of OCI and the vicarious orbital sensor. Figure 6 depicts the method of registration for OCI against the SeaWiFS. The method shown is composed of an image registration and a data set registration. Commanding the two sensors to take images near in time (morning time around 11 o'clock for the OCI and SeaWiFS) over some surface site where their nadir tracks cross each other does the image registration. Extracting the required data around the cross point of the nadir tracks from each of the images is the data set registration. The data set registration can be achieved by image processing or other computer aided data handling on the ground segment. As mentioned before the registered data sets from each of the images should have the same ground coverage over the cross point. If the surface site around the cross point is homogeneous and uniform in reflectance, the same ground coverage in area instead of perfect matching will be accurate enough for the calibration. The image registration needs to have the parameters of the orbits and pointing of the two sensors (satellites), so that the time and coordinates of the cross points can be computed in advance for setting up the imaging commands. Alternatively a particular surface site can be chosen for the cross-platform calibration, but the data will not be available until the two sensors fly over there near in time. However if vicarious calibration based on measurements of surface reflectance is done within the same site, the result of calibration can be double-checked.

5.2 Cross-band In-flight Calibration

Bands 4 and 7 of OCI observe through different telescopes but are spatially well co-registered and spectrally redundant. Thus they will be able to observe simultaneously the same surface targets through the same atmosphere. By comparing both sets of data, a function of fault detection can be developed to determine when to switch the on-duty band. The fault detection is designed to check the following parameters:

$$\beta_{b_{4,7}p}(t) = \frac{\left|\hat{L}_{b_4p}(t) - \hat{L}_{b_7p}(t)\right|}{Max\{\hat{L}_{b_4p}(t), \hat{L}_{b_7p}(t)\}} \tag{17}$$

where $Max\{\hat{L}_{b_4p}(t), \hat{L}_{b_7p}(t)\} \neq 0$. A fault is detected if

$$\beta_{b_{4,7}p}(t) \geq \varepsilon \tag{18}$$

where ε, $0 \leq \varepsilon < 1$ is a specified threshold. Detection of a fault will request a calibration to these two bands so that the abnormal band can be identified.

When no fault is found, Band 4 can be calibrated with respect to Band 7 or vice versa. This may happen when one uses either NI-A or NI-B mode to collect data for the in-flight calibration, and invokes a CA mode imaging to provide data for cross-band calibration between Band 4 and 7. For the cross-band calibration, the offsets are calibrated as described before. However since pixel by pixel cross-calibration is possible, the relative sensor gains are assessed by (10) or more specifically as follows:

$$\alpha_{b_4 p}(t) = \frac{\widehat{C}_{b_4 pg}(t) - \widehat{D}_{b_4 pg}(t)}{gF_{b_4 p}(t_0)\widehat{L}^{v}_{b_7 p}(t)} \tag{19}$$

for Band 4 with respect to Band 7, and

$$\alpha_{b_7 p}(t) = \frac{\widehat{C}_{b_7 pg}(t) - \widehat{D}_{b_7 pg}(t)}{gF_{b_7 p}(t_0)\widehat{L}^{v}_{b_4 p}(t)} \tag{20}$$

for Band 7 with respect to Band 4. To account for the uncertainties, each relative sensor gain is assessed as the average of the answers from either (19) or (20) for more than one scanning line.

6. A SENSOR CALIBRATION ALGORITHM OF OCI

Figure 7 shows a block diagram of the sensor calibration algorithm for OCI, where L1A (i.e., level 1A) denotes the OCI output data in digital counts, and L1B (i.e., level 1B) corresponds to the calibrated at-sensor radiance data. The algorithm is essentially composed of two subsystems as parameter adaptation and data conversion. A parameter pool maintains the pre- and in-flight parameters and plays as an interface between the two subsystems. In the figure the SeaWiFS is assumed as the vicarious orbital sensor of cross-platform in-flight calibration. The pre-flight parameters including the sensor gains and offsets are measured before launch and saved in the parameter pool. The in-flight offsets are obtained from the OCI L1A data by night observations for each band and gain selection. The corresponding blocks in Figure 7 depicts an example of the required operating mode, gains and pixels. In the cross-platform calibration, OCI and the vicarious orbital sensor are commanded to acquire data over the same target site (i.e., cross-point) near in time so that the sun-sensor geometry will be similar. The vicarious orbital sensor has to have well calibrating procedure to ensure the accuracy and quality of the calibrated at-sensor radiance data. The calibrated at-sensor radiance data obtained by the vicarious orbital sensor are compared with the corresponding OCI data to assess the in-flight relative sensor gains. The data registrations locate the data sets that cover the same ground area over a cross point and select appropriate number of pixels to do the cross comparison. In Figure 7, the OCI and SeaWiFS are shown to select 11x11 and 8x8 pixels, respectively. Except the registration of data sets, the computations are mainly described by (12)~(16). When cross-band fault detection and calibration between Band 4 and 7 are adopted, (17)~(20) are extra formulas for computation. The cross-platform in-flight calibration can be held monthly or frequently, and the calibrated parameters with time stamps are stored in the parameter pool. In the data conversion, the input is the OCI L1A data with time stamp for searching appropriate parameters from the parameter pool. The output is the calibrated at-sensor radiance data computed by using (6). The algorithm mentioned above has been implemented as a software package entitled OCICAL and available for the OCI applications.

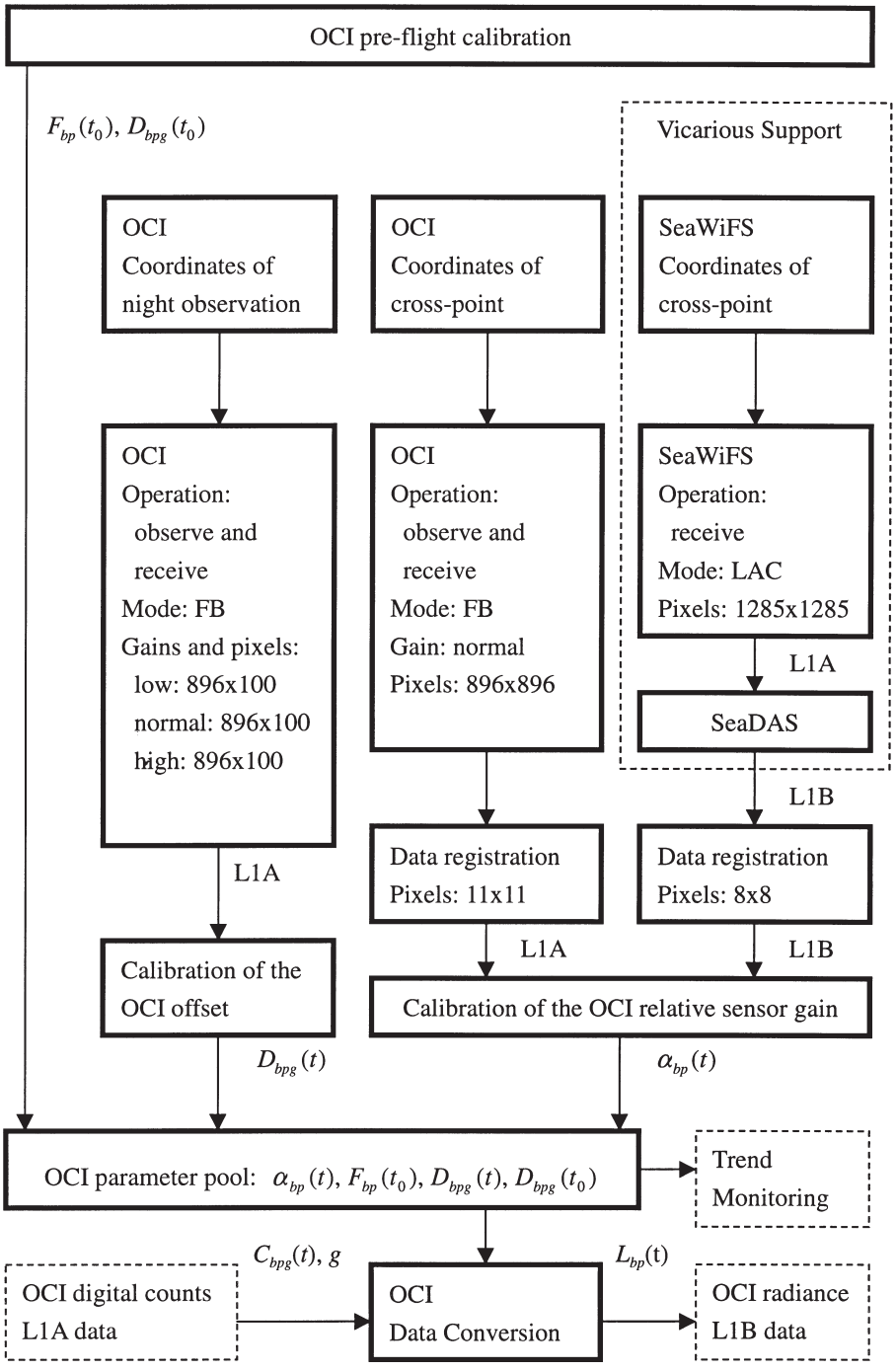

Fig. 7. An algorithm of the OCI parameter adaptation and data conversion, where SeaDAS is a software package for the SeaWiFS data processing.

7. CONCLUSIONS

OCI has been successfully built and parameterized, and is ready for launch (i.e., January 27, 1999). This paper provides a summary of the major engineering data as well as a method of sensor calibration so that the follow-up applications can progress smoothly. Technically, OCI is a compact pushbroom scanner without any moving or rotating components so that highly reliable performance is expected. However, being without any on-board calibrator, it is important to monitor the short- and long-term variations of the performance for vicarious in-flight calibration. Among the reflectance- and radiance-based vicarious calibrations, cross-platform in-flight calibration using the calibrated top of the atmosphere radiance measured by vicarious orbital sensor over the target site seems to be a convenient approach for OCI. Fortunately the spectral bands of OCI were selected to match or overlap with those chosen by some on-duty ocean color sensors such as SeaWiFS and MODIS. This undoubtedly motivates the sensor calibration to take advantage of the well-calibrated radiance data obtained by these spaceborne sensors. The proposed sensor calibration has characterized OCI's radiometric response and developed a method of data conversion integrated with the cross-platform in-flight parameter adaptation. Future work will check the results with other reflectance- and radiance- based vicarious methods of in-flight calibration.

Acknowledgements This work is one of the projects of the OCI Science Team supported by the National Space Program Office of the National Science Council under NSC-86-NSPO-A-OCI-019-01-03 and NSC-87-NSPO-A-OCI-019-01-03. W. S. Lin would like to acknowledge the support from Mr. Y. Narimatsu and the members of the NEC Space Systems Division in Yokohama, Japan. The authors wish to acknowledge the support from the members of the OCI team of the National Space Program Office in Taiwan.

REFERENCES

Che, N. B., B. G. Grant, D. E. Flittner, P. N. Slater, S. F. Biggar, R. D. Jackson and M. S. Moran, 1991: Results of calibration of the NOAA-11 AVHRR made by reference to calibrated SPOT imagery at White Sands, N. M. *SPIE: Calibration of Passive Remote Observing Optical and Microwave Instrumentation*, **1493**, 182-194.

Gordon, Howard R., 1998: In-orbit calibration strategy for ocean color sensors. *Remote Sensing and Environment*. **63**, 265-278.

Hooker, S. B., W. E. Esaias, G. C. Feldman, W. W. Gregg, and C. R. MeClain, July 1992: SeaWiFS technical report series volume 1, An overview of SeaWiFS and Ocean Color. Technical Memorandom 104566, NASA, Greenbelt, MD.

Johnson, B. C., F. Sakuma, J. J. Butler, S. F. Biggar, J. W. Cooper, J. Ishida and K. Suzuki, 1997: Radiometric Measurement Comparison Using the Ocean Color Temperature Scanner (OCTS) Visible and Near Infrared Integrating Sphere. Manuscript.

Narimatsu, Y., et al., 1997a: Ocean Color Imager Instrument, critical design review." NEC Space Systems Division. OCI-BS-244-NEC, 8-22.

Narimatsu, Y., et al., 1997b: Rocsat-1 Program: Ocean Color Imager FM delivery data pack-

age. NEC Space Systems Division. OCI-BS-037-NEC.

Narimatsu, Y., et al., 1997c: ROCSAT-1 Ocean Color Imager calibration report. NEC Space Systems Division. OCI-BS-039-NEC.

NSPO OCI Team, May 1993: Ocean Color Imager for ROCSAT: feasibility study final report. MMS/OCI/NT/93-032.

Ono, A., F. Sakuma, K. Arai, Y. Yamaguchi, H. Fujisada, P.N. Slater, K.J. Thome, F. D. Palluconi and H.H. Kieffer, April 1996: Pre-flight and in-flight calibration plan for ASTER. *J. Atmos. Ocean. Tec.*, **13**, **2**, 321-335.

Rao, C. R. N. and J. Chen, 1994: Post-launch calibration of the visible and near infrared channels of the Advanced Very High Resolution Radiometer on NOAA-7, -9 and –11 spacecraft. Washington D.C.: National Oceanic and Atmospheric Administration, no. NESDID 78.

Salomonson, V. V., W. L. Barnes, P. W. Maymon, H. E. Montgomery and H. Ostrow: MODIS, 1989: advanced facility instrument for studies of the Earth as a system. *IEEE Geoscience and Remote Sensing*. **27**, 145-152.

Schowengerdt, Robert A., 1997: Remote Sensing: Models and Methods for Image Processing. Academic Press. a: 310-318, b: 69-94.

Slater, P. N., S. F. Biggar, R. G. Holm, R. D. Jackson, Y. Mao, M. S. Moran, J. M. Palmer and B. Yuan, 1987: Reflectance- and radiance-based methods for the in-flight absolute calibration of multi-spectral sensors. *Remote Sensing and Environment*. **22**, 11-37.